Proton radius measurement using μp elastic scattering at COMPASS

Stephan Paul, Sebastian Uhl, Jan Friedrich, Norbert Kaiser,....

September 19, 2017

1 Introduction

The determination of the size of the proton, the most abundant hadron in our Universe, has been in the focus of intensive research since more than 60 years [1](see fig. 1 for the history of the proton charge radius). Unlike the protons' electric charge or magnetic moment, which have been determined with high precision, the charge distribution of the proton and thus its mean square charge radius is badly known and has recently been at the origin of very active research program pursued at various laboratories. Traditionally, charge distributions are measured using low energy elastic electron scattering and the measurements for the protons have made use of the Rosenbluth separation of the electric and magnetic form factors. The results of this method had been challenged about 7 years ago using high-precision muonic-hydrogen spectroscopy [2, 3] performed at PSI (see fig. 2).

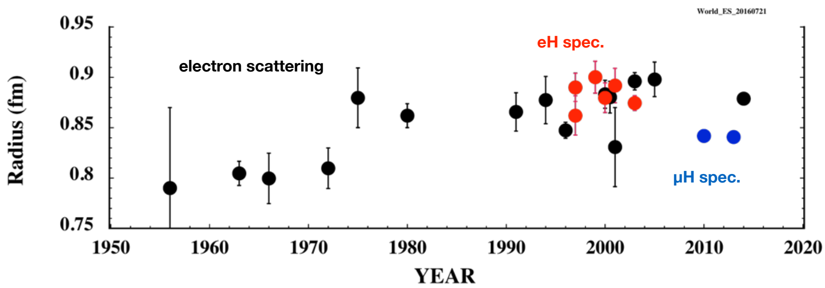

Figure 1: Historical development of the proton charge radius. Figure is taken from [9].

Despite much experimental efforts over the last years, the resulting proton radius puzzle [10] has been plagued physicists ever since. At MAMI, an admirable experimental effort to address the proton radius using elastic ep scattering down to Q^2 of about $10^{-3}(GeV/c)^2$ has basically confirmed older electron scattering results [4]. These efforts were motivated by the suspicion, that the extrapolation of scattering data down to $Q^2 = 0$ might carry unknown uncertainties related to either experimental flaws of the measurements at higher values of Q^2 or by yet unknown physics changing the slope of the differential cross section towards very small momentum transfers. New experiments are planned or under way [5], which aim extending the lowest values of Q^2 down to $2-5\cdot 10^{-4}(GeV/c)^2$ [7] (data taken in 2016)[6]. Here, detected initial state radiation is used to lower the range of Q^2 as compared to previous measurements at MAMI. Yet another experimental proposal at MAMI employs an alternate experimental approach determining Q^2 from the proton recoil alone (supplemented by the more standard measurement of the outgoing electron). Although the measurements uncertainties connected to electron scattering experiments strongly mismatches the spectroscopical results, the discrepancy in the proton radius determined by muonic hydrogen and *ep* elastic scattering is a multiple of this uncertainty.

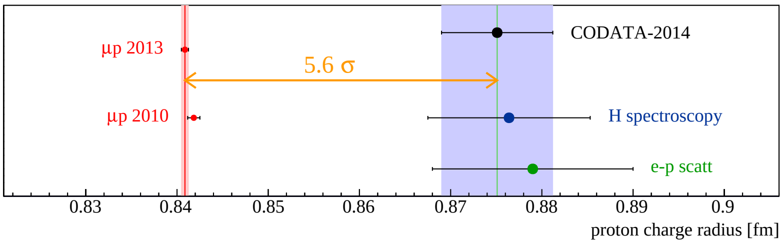

Figure 2: Proton charge radius from muonic hydrogen (red), hydrogen spectroscopy (blue) and electron-proton scattering (green). The CODATA value accounts for e-p scattering, H and deuterium (D) spectroscopy but does not consider the muonic results. Figure is taken from [11].

Until recent, also the spectroscopy of electronic hydrogen differed from the muonic one, though by less than *ep* scattering data, and there has been a call to investigate the last missing experimental measurement, elastic μp scattering. Very recent spectroscopical data on muonic deuterium lead to a new determination of the Rydberg constant ($R_\infty^{\mu d} = 3.289841960234(6) \cdot 10^{15}$ Hz/c)[1][13]. For this, atomic transition to higher lying states ($2s \to nl$) had to be considered, which in case of electronic hydrogen lead to inconsistent results among various transitions. Averaging these results lead to the Rydberg constant used to extract the proton radius from the Lamb-shift measurements ($2S \to 2P$) as $R_\infty^{CODATA-2010} = 3.289841960355(19) \cdot 10^{15}$Hz/c. The new determination of the Rydberg constant was used to reinterprete all electronic hydrogen data, which now brings muonic and electronic hydrogen into agreement (see fig. 3). This situation has now put more weight on the issue of lepton scattering versus spectroscopical radius measurement and quests for very low Q^2 data. Here, high energy muons are an ideal tool owing to reduced systematics from multiple scattering and Bremsstrahlung corrections.

In addition to a very active discussion concerning the two different measurement methods there are debates on the proper analysis of electron scattering data. Bernauer and Distler, co-authors of the Mainz measurements, give a detailed explanation on the techniques of model fitting on the electron scattering data [14], firmly concluding to the large value for the proton radius. On the other hand, [15, 16] argue from a theoretical point of view on the unphysical parametrisation of form factors used by the experimentalists, leading to a false slope of the form factors at $Q^2 = 0$. Indeed, their fit of the electron scattering data using a dispersive approach for the form factors results in proton charge radius very well compatible with the spectroscopical data.

The present situation asks for a new measurement using a different experimental Ansatz and covering a wide range of Q^2. The low Q^2 region is vital to constrain the parametri-

[1]there is a 2.2σ difference between $R_\infty^{\mu D}$ and $R_\infty^{\mu H}$

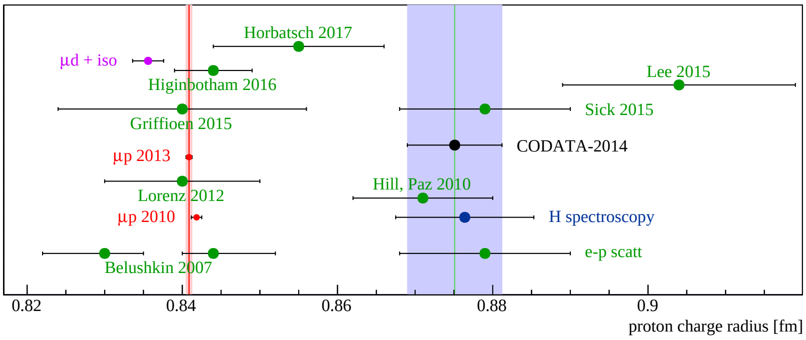

Figure 3: Proton charge radius from muonic hydrogen (magenta), the new hydrogen spectroscopy data (green) and former electronic hydrogen spectroscopical data (blue). The CODATA value accounts for e-p scattering, H and deuterium (D) spectroscopy but does not consider the muonic results. Figure taken from [12, 13]. All hydrogen data have been rescaled using the value for the Rydberg constant extracted from muonic deuterium spectroscopy. The latter also allows to extract a value for the proton radius using the H-D isotope shift (magenta).

sation of the form factors and thus give more comfort for their extrapolation to $Q^2 = 0$. A lower limit of $Q^2 = 10^{-4}$ is desirable. On the other hand, the region of large Q^2 gives sensitivity to the charge radius.

The MUSE [17] experiment at PSI has recently been set-up to perform a first precision experiment on elastic μp scattering, investigating with the same apparatus elastic scattering of both muon charge states, electrons and positrons. As these measurements are performed at very low values of Q^2, beam intensity is not an issue, unlike for form factor measurements at high Q^2, where continuous electron beam machines like JLAB or MAMI are without alternative. The PSI experiment MUSE aims at accuracies, which are compatible with older electron beam data (check this), which is mainly caused by the low μ-beam energies at PSI (check list of quoted uncertainties of MUSE). The kinematic range in Q^2 for MUSE is $0.0016 - 0.0799$ $(\mathrm{GeV/c})^2$ and is almost the same for electrons and muons. The largest uncertainties from this measurement will come from muon decay corrections (before or after the scattering process) and radiative corrections. The statistical uncertainties of the cross sections range from about 0.3 to 1% at the larger scattering angles. The systematic uncertainties are at about the 0.5% level, thus systematic uncertainties are expected to slightly outweigh statistical ones. For each particle species they thus expect an accuracy of their measurement of 0.01 fm, possibly even 0.006 fm, depending on the analysis method.

The μ beam flux at PSI varies between $0.2 - 6 \cdot 10^6/s$ and is beam charge and energy dependent. It it has typically below the muon beam intensities achieved at COMPASS. While at COMPASS the μ-beam is pure at the level of $10^{-5} - 10^{-6}$ on what concerns pion contamination, electrons constitute the largest background for MUSE being a factor 10-100 more abundant than muons. Similar numbers hold for pion background.

Very recently, a new experiment has been proposed at Tohoku Univ. (Japan) aiming at very low energy scattering of electrons from protons in order to address the smallest region of $Q^2 > 0.0003(\mathrm{GeV/c})^2$. Electron beam energies between 20-60 MeV are planned impinging on a hydrogen target with carbon admixture for luminosity measurements.(unfortunately, I do not know more details)

2 A μp elastic scattering experiment at COMPASS

In light of the experimental situation outlined above, it seems desirable, to perform a highly competitive elastic proton scattering measurement with high energy muons within the COMPASS experiment at CERN, which combines most of the above mentioned improvements of individual experimental efforts.

- a high intensity muon beam
- a high energy beam for low multiple scattering effects
- easy beam charge flips to measure both μ^+ and μ^- scattering
- high resolution in Q^2 of a few $10^{-4}(GeV/c)^2$, as demonstrated by pion Primakoff scattering [20]
- employment of an active target, to allow for precise proton recoil measurement
- possibly reference measurements to prove control of the experimental luminosity (e.g. μe elastic scattering)
- possibility to employ a high energy electron beam at the same beam line (details to be investigated)[18]

2.1 Kinematics

The differential Mott cross-section for elastic lepton scattering on nucleons is given by [19]:

$$\begin{aligned}\frac{d\sigma}{dt} = \frac{4\pi\alpha^2(\hbar c)^2}{t^2}\Bigg\{\left[\frac{(s+M^2-m^2)^2}{4M^2-t}+m^2-s\right]\left[4M^2G_E^2(Q^2)-t\;G_M^2(Q^2)\right] \\ +t\Big(m^2+\frac{t}{2}\Big)G_M^2(Q^2)\Bigg\}\frac{1}{s-(M+m)^2}\;\frac{1}{s-(M-m)^2}\end{aligned} \tag{1}$$

where t $= -Q^2$ is the momentum transfer squared and s is the center of mass energy squared. Target and beam particle masses are denoted by M and m. The cross section is characterised by the electric and magnetic form factors $G_E(Q^2)$ and $G_M(Q^2)$. At small values of four momentum transfer these form factors are typically written in terms of the nucleon electric charge radius r_e expanded in powers of Q^2 [14]:

$$G_E(Q^2)/G_E(Q^2=0) = 1 - \frac{1}{6} < r_e^2 > Q^2 + \frac{1}{120} < r_e^4 > Q^4 - \frac{1}{5040} < r_e^6 > Q^6 \tag{2}$$

and the mean of the charge-radius squared can be extracted from the slope of the form factor at zero Q^2:

$$< r_e^2 >= -6 \cdot \frac{dG_E(Q^2)}{dQ^2}\Big|_{Q^2=0} \tag{3}$$

The Q^2 dependence of the cross section is shown in fig. 4a. As the expansion of the form factors in terms of $<$ r$_e^2$ $>$ is only working for small values of Q^2, we also show the differential cross section using the dipole form-factor up to larger values of Q^2 fig. 4b. The sensitivity of the cross section for different values of the charge radius is depicted in fig. 5, where we show the cross section ratio for two extreme values of $\sqrt{<r_e^2>}$ with 0.84 fm and 0.88 fm. Although it is assumed that measuring down to very small values of Q^2 reduces uncertainties extrapolating the measured cross section down to $Q^2 = 0$, sensitivity to finite size effects can only be obtained at higher values of Q^2.

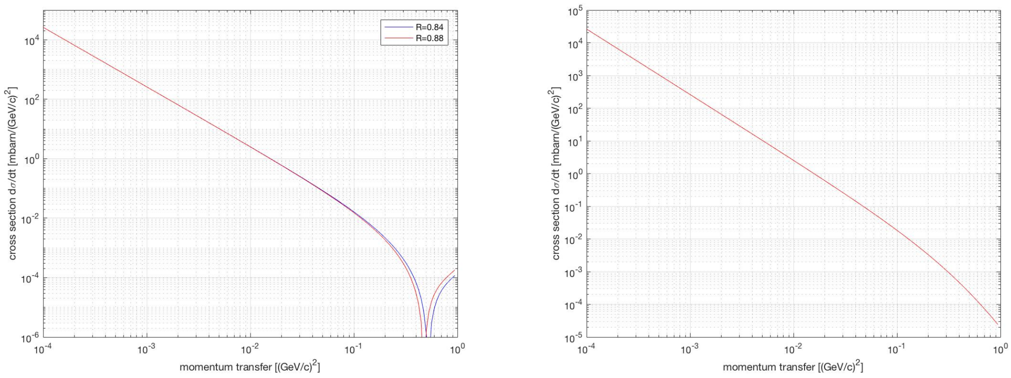

Figure 4: Q^2 dependence of the μp elastic scattering cross section for different form factor parametrizations. Left: form factor expansion in powers of Q^2 and $\sqrt{<r_e^2>}$ (see eq. (2)) assuming a $\sqrt{<r_e^2>}$ of 0.84 fm and 0.88 fm. Right: assuming a dipole form-factor (see eq. (3)).

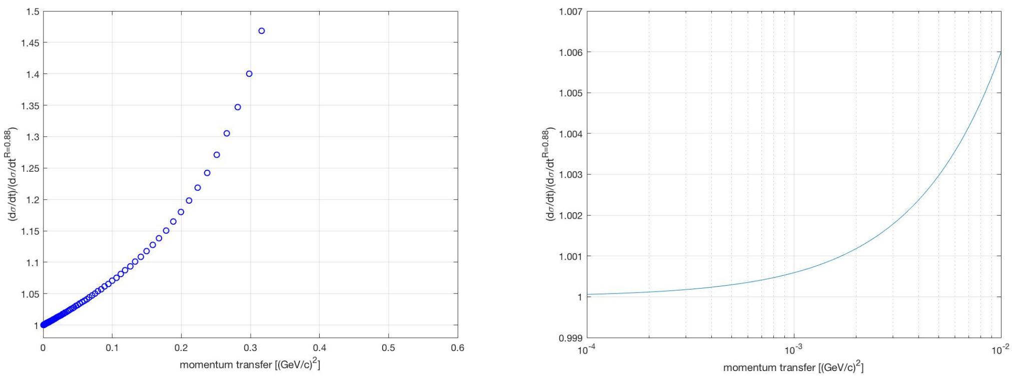

Figure 5: Ratio of cross sections for $\sqrt{<r_e^2>}$ with 0.84 fm and 0.88 fm (denoted as σ_0). Left: for large values of $(\mathrm{GeV/c})^2$ (linear scale), right: zoom for low $(\mathrm{GeV/c})^2$ (semi-log scaling).

2.2 Requirements deduced from scattering kinematics and cross section

In order to design the experimental set-up we need to understand the scattering kinematics. Figure 6 and fig. 7a show the Q^2 dependence of energy and scattering angle of the scattered muon. Figures 8 and 9 the corresponding distributions for the recoil proton. For the proton the scattering angle is calculated w.r.t. the normal of the incoming beam. In elastic scattering, recoil energy and angle are correlated and are shown in fig. 10. All kinematic quantities only depend on Q^2 and are almost independent of the

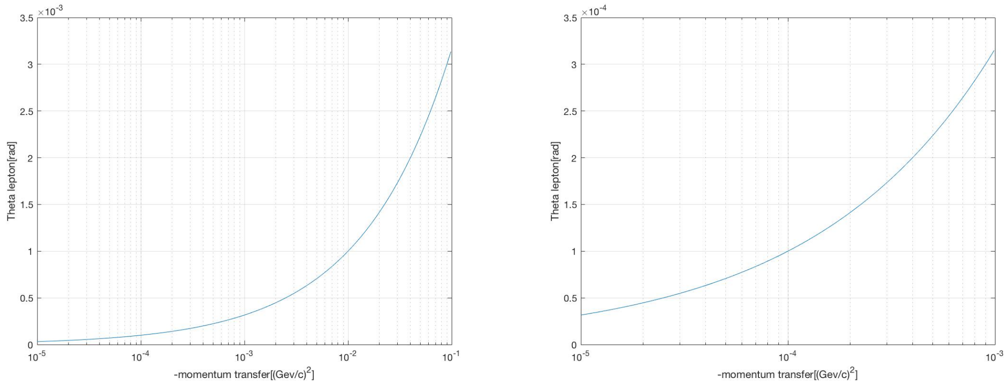

Figure 6: Q^2 dependence of the muon scattering angle for elastic μp scattering assuming 100 GeV beam energy

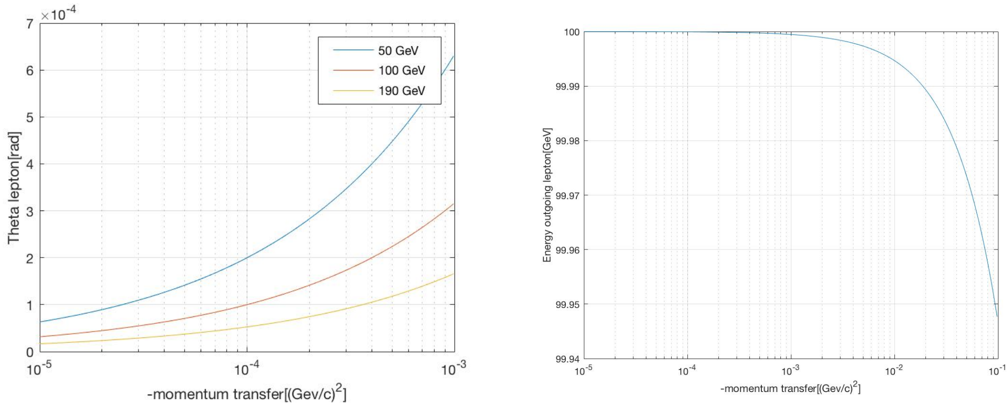

Figure 7: Left: Q^2 dependence of the muon scattering angle for elastic μp scattering assuming three different beam energies of 50, 100 and 190 GeV. Right: Q^2 dependence of the energy of the outgoing muon assuming 100 GeV beam energy.

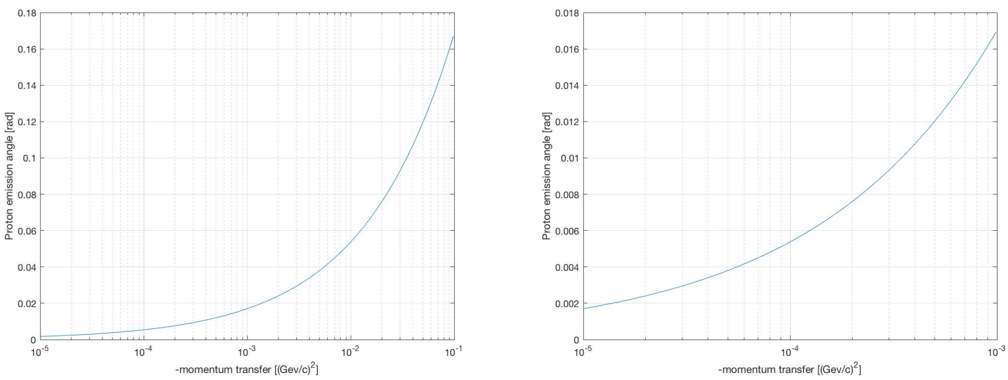

Figure 8: Left: Q^2 dependence of the proton scattering angle (measured w.r.t. the normal of the beam direction) for elastic μp for different intervals of Q^2.

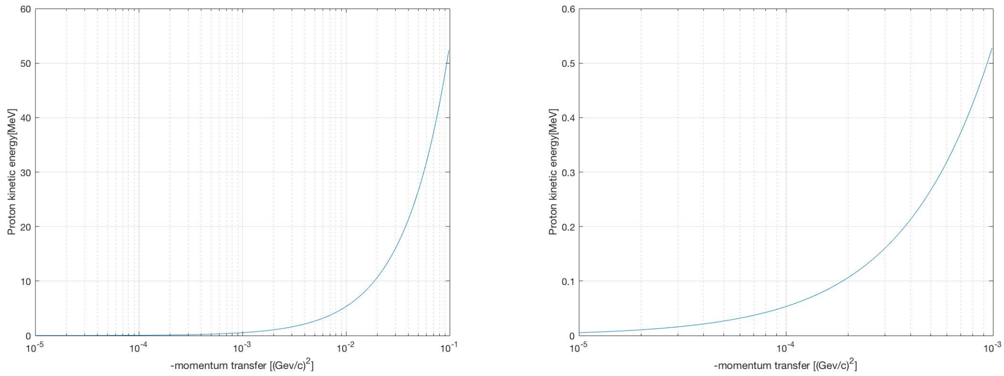

Figure 9: Q^2 dependence of the energy of the outgoing proton assuming 100 GeV beam energy for different intervals of Q^2.

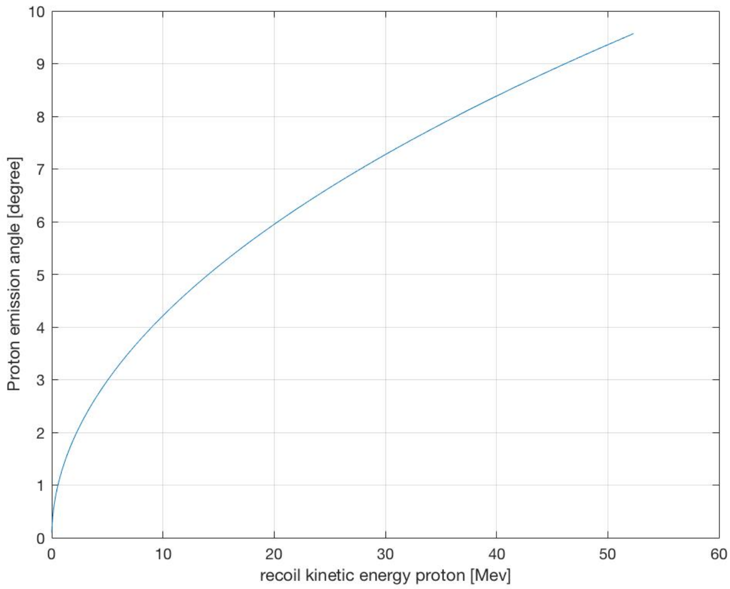

Figure 10: Correlation of proton emission angle (measured w.r.t. the normal of the beam direction) and proton kinetic energy.

beam energy, except for the muon scattering angle shown in fig. 6b for three different possible values of the incoming muon energy.

At a beam energy as large as 100 GeV typical magnetic spectrometers have energy resolutions of a few ‰ being insufficient to determine Q^2, which thus has to be determined from the muon scattering angle alone. However, scattering angles are small and typical far below the beam divergence. This imposes new triggering schemes in order to reach values for $Q^2 \approx 10^{-4}(GeV/c)^2$.

The recoil proton is emitted mostly perpendicular to the beam at about 90° and reaches 10°with respect to the beam normal for higher values of $Q^2 \approx 10^{-1}(GeV/c)^2$. Small values of Q^2 result into small proton energies where the determination of the scattering angle will be difficult. Thus, the measurement of the recoil angle cannot be used to determine Q^2 or act as a trigger signal. However, the proton recoil energy varies from 50 keV to 50 MeV for $10^{-4} < Q^2 < 10^{-1}(GeV/c)^2$. It may thus be used as secondary measurement of Q^2 for most of the range of interest.

3 Experimental set-up

The experimental set-up uses the standard muon beam set-up of COMPASS, but the target region will be modified as to accommodate an active hydrogen target, possibly an active SciFi target and two silicon telescopes. It is depicted in fig. 11. The active hydrogen target (ICAR [26]) is based on an existing setup used for an experiment at GSI, which is shown in fig. 12. Such a system has been developed by the Gatchina group (PNPI), and which has been employed for multiple radius measurements over the past.

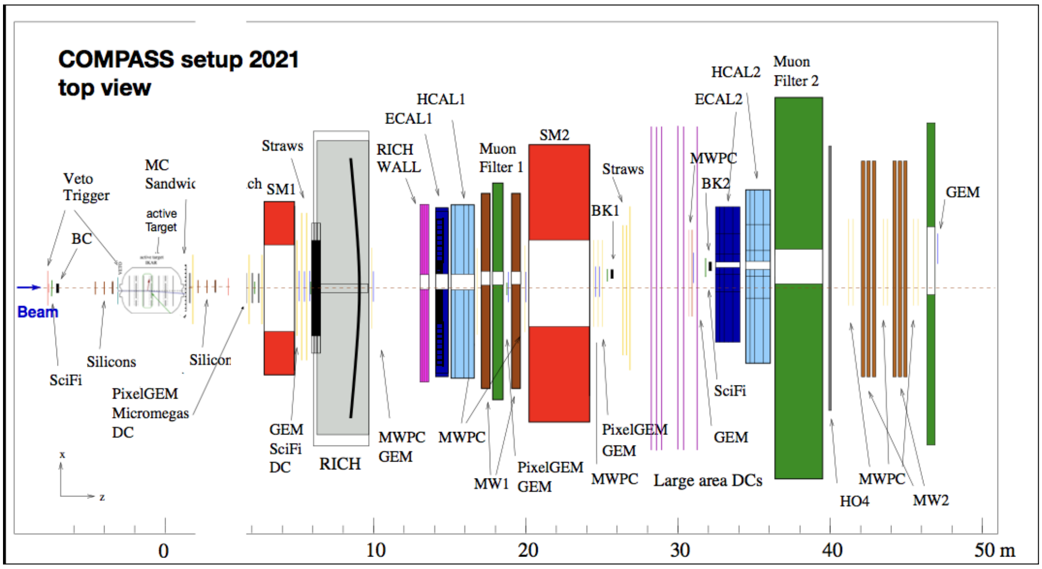

Figure 11: Schematics of the COMPASS MUP setup. The target region including the gaseous hydrogen TPC is not to scale.

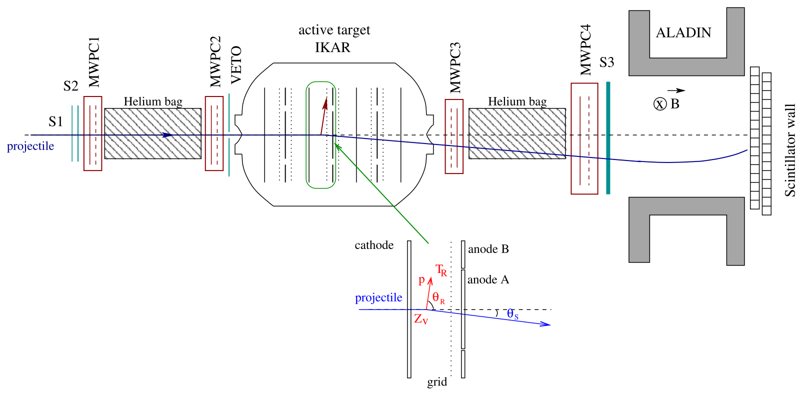

Figure 12: Example for the use of a high pressure active target TPC [26]

3.1 Proton measurement

The proton recoil measurement can be achieved using a double target scenario. For small values of Q^2, with proton kinetic energies up to a few MeV, we can use a high pressure hydrogen TPC operated as ionisation chamber. At higher values of Q^2 one may envisage an active target made from scintillating fibres.

3.1.1 A pressurised hydrogen filled Ionization TPC

Since the very beginning of elastic scattering experiments with leptons, high-pressure, thin-wall gas chambers were used as targets, the design of which was pioneered by Eva Wiener[2]. An example for an experiment using such a device is shown in fig. 12 [26]. Such targets have been turned into an active target/detector system by the Gatchina group (PNPI) [25], and have been employed for multiple radius measurements over the past. The energy dependence of the specific energy loss and range for recoil protons in hydrogen gas at a working pressure of 4 bar are shown in fig. 16. The energy dependent specific energy loss for the muon is shown in fig. 18. The energy loss for incoming and outgoing muons is about 2 keV/cm and thus small as compared to the proton energy loss even for proton kinetic energies of 10 MeV, as long as the path length traversed is below 10cm.

For $Q^2 = 10^{-4}(GeV/c)^2$, the kinetic energy of recoil protons is 50-60 KeV. This value corresponds to the energy resolution obtained by [25] in an experiment measuring πp scattering in the Coulomb-nuclear interference region. This roughly determines the scale for lowest value of Q^2 in the experiment.

A key issue for the TPC is the maximal drift time. This determines the effective gate length and thus the overlay of non-interacting beam particles.

The 60 cm long hydrogen-gas volume is divided into slices of 20 cm, each one forming a TPC with drift in longitudinal (beam) direction. Unlike in most other cases the TPC will be operated in ionisation mode. This avoids statistical fluctuations in the amplification process and thus allows for high energy resolutions. The latter is only determined by fluctuations in the primary ionisation. Resolutions of 50 keV have been

[2] a PhD student of R. Hofstaedter and who died in a car accident during her thesis work

obtained in NA8 at beam intensities of 10^6. The design of the TPC is motivated by the exact knowledge of the fiducial volume for reconstructable elastic scattering events. This requires high precision on the gas density and geometrical parameters, the exact characterisation of the active TPC volume. Details on the construction and calibration of the TPC can be found in appendix A.1 (see fig. 13).

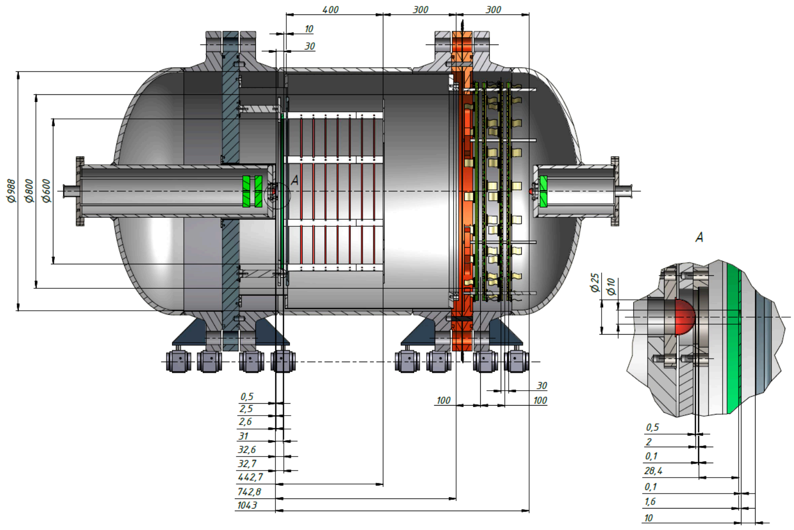

Figure 13: Sketch of the target TPC with pressure vessel as conceived for an elastic $e^{-}p$ scattering experiment at MAMI. The forward tracker system on the right side of the vessel will not be installed for COMPASS.

Resolutions

As the hydrogen gas volume is segmented into 4 independent TPC sections we need to identify the TPC section for the scattering. The longituidinal vertex resolution using the scattered muon alone is sufficient for $\mathrm{Q}^2 > 4 \cdot 10^{-3}$. Measuring smaller momentum transfers requires the information from the recoil proton measured within the TPC. This can be done requiring a minimum energy deposit detected in a TPC segment of $> 3 \cdot \sigma_{noise}=$ 150-200 keV. Using more sophisticated algorithms considering the pulseheight pattern observe in all TPC segments could possible lower this limit, which however ist not crucial for this measurement.

We have performed first simulations on the achievable Q^2 resolution using the ionisation TPC. The results are shown in fig. 15. We assume the setup for the target region depicted in fig. 15a. Each silicon station is assumed to be of the type used for Primakoff measurements performed previously within COMPASS. However, the spacing of the stations has been enlarged to 1m for both beam and spectrometer telescope. In fig. 15b) we show the achievable relative Q^2 resolutions for different values Q^2. For silicon alone, we use the standard COMPASS track reconstruction algorithms. For the Q^2 reconstruction within the TPC we assume an energy resolution for the kinetic recoil proton energy of ... keV. We also show the results for the combined reconstruction. We conclude that we can perform measurements for elastic μp scattering down to $\mathrm{Q}^2 \approx 10^{-4}(\mathrm{GeV/c})^2$.

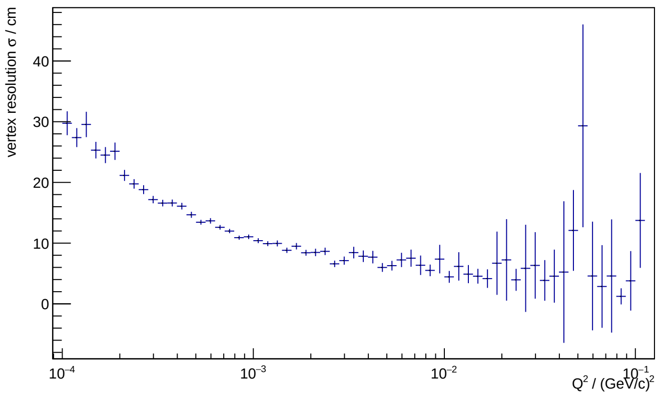

Figure 14: Longitudinal vertex resolution σ_z for a reconstruction only based on incoming and scattered muon.

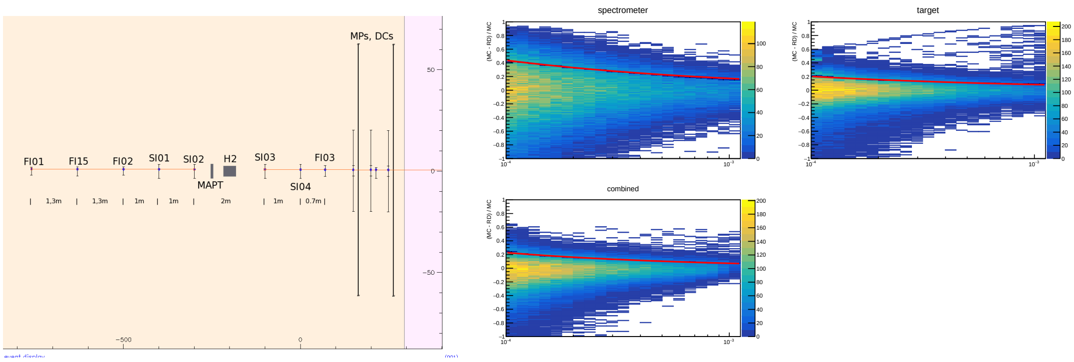

Figure 15: Left: setup of the target region used for resolution studies. Downstream of this region, the full standard COMPASS spectrometer is assumed. Right: Projected relative Q^2 resolutions using two silicon telescopes and an ionisation TPC fill with hydrogen gas at 4 bar pressure. The contribution from each detector is shown separately as well as the combined information.

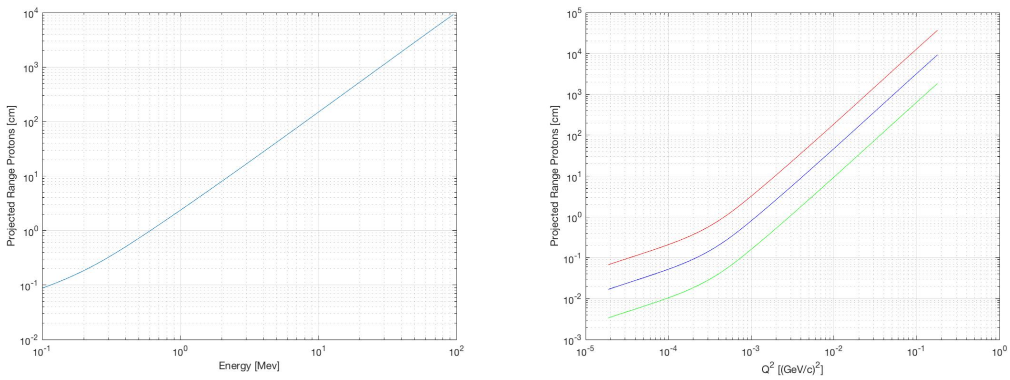

Figure 16: Projected range for protons in hydrogen gas. Left: hydrogen at 4 bar pressure for different kinetic energies [34]. Right: in hydrogen at 1 bar (red), 4 bar(blue) and 20 bar(green) for different Q^2.

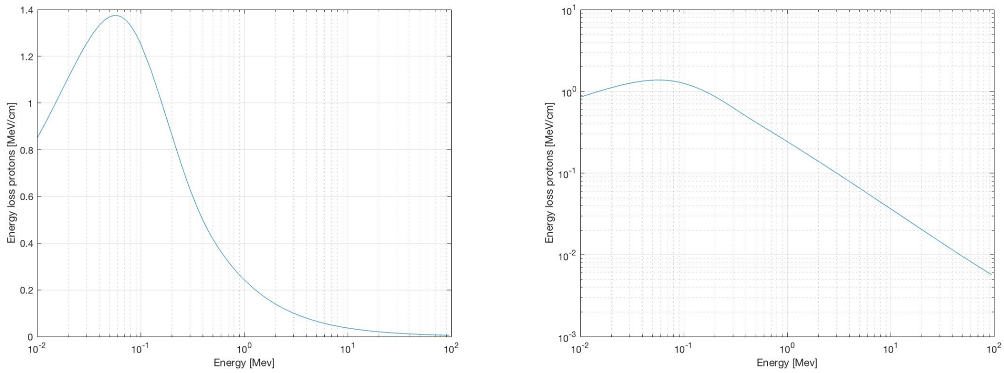

Figure 17: Projected range (left) and specific energy loss (right) for protons in hydrogen gas at 4 bar pressure for different kinetic energies [34].

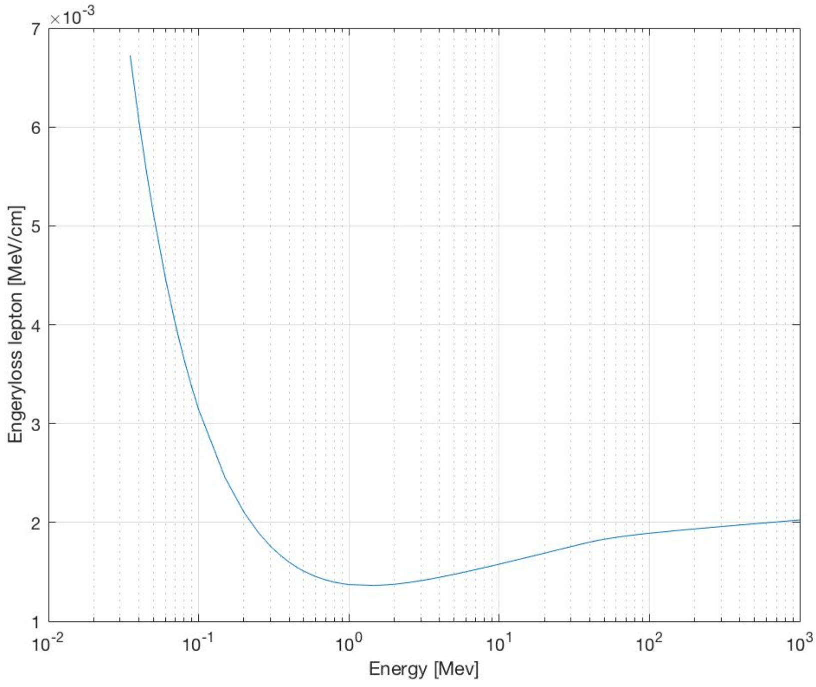

Figure 18: Specific energy loss for muons in hydrogen gas at 4 bar pressure for different kinetic energies [34].

3.1.2 An active scintillating fibre target

For higher values of Q^2 we envisage to use an active target made from scintillating fibres arrange vertically to the beam direction. The target fibres are surrounded by longitudinally stretch fibres arrange on a cylinder along the beam direction. Consecutive layers are arranged in a relative stereo angle of 6° . A possible setup is shown in fig. 20. The scintillation light form the fibres is detected on one side by SiPM of high pixel density (Hamamatsu S13360-3025 or KETEK PM3325) to reduce saturation effects. The backend opposing the SiPM is aluminised. In the model used for simulation we assumed 10 layers of scintillating fibres, summing up to 2cm thickness. In order to perform a combined (dE/dx,E) analysis, we intend to surround the fibre tracker by 8 plates of scintillator, similar to the proton recoil detector surrounding the liquid hydrogen target of COMPASS in 2009. With this, we should be able to stop protons up to 100 MeV. Figure 19 shows both range and specific energy loss pf protons in scintillator made from vinyltoluene-based material. By reconstructing the Bragg curve (fig. 21a we can obtain energy resolutions in the range of % (fig. 21b). We have performed test measurements on energy resolution up to energies of about 50 MeV at PSI using various fibre material and models of SiPM. First results from the analysis are expected soon.

As the range of low energy protons in the SciFi material is low we need to keep the fibre thickness small in the inner layers ($2 \times 2\ mm^2$). A requirement for the recoil proton of crossing at least 2 fibres to determine a 3D impact point imposes a lower limit for the kinetic energy of recoil protons of about 15-20 MeV. This corresponds to a lower value of $Q^2 >$ 0.03-0.04 $(\mathrm{GeV/c})^2$, as can be read from fig. 9. The fibre cross-section for the outer layers may grow to $4 \times 4\ mm^2$ and $8 \times 8\ mm^2$.

In order to reduce multiple scattering, the length of the fibres in the beam should be about 1cm and extended to the forward direction outside of the centre. With the beam of about $5 \cdot 10^7 \mu/\mathrm{s}/cm^2$ we need to reduce the size of the central fibres to 1 mm. This limits the individual rates to $5 \cdot 10^5 \mu/\mathrm{s}/\mathrm{fibre}$. As SiPM and connected electronic circuitry have a dead time of about 200ns, this should reduce dead time corrections (one might further decrease the dead time with suitable shapers for the preamps.).

The use of a solid target infers quasielastic scattering events to spoil the data sample. However, they constitute a partly reducible background. Owing to the quasi elastic kinematics, good energy and angular resolution for the recoil proton allows a rejection by about a factor 100 up to $Q^2 < 0.3(GeV/c)^2$. This background is discussed in detail in appendix A.3. Considering a SciFi composition of $(CH)_n$, the quasi elastic background would be six times higher than the elastic signal. As the cross section for the two different radii considered is about 10-20% above $Q^2 > 0.1(GeV/c)^2$ as depicted in fig. 25b), this limits the accessible range of such a measurement.

The readout of SiPM can be performed using a TDC ASICs (CLARO-CMOS developed for the upgraded LHCb RICH detector) or IDE3380 SIPHRA (developed for SiPM in space usage) and performing time over threshold analysis. Performance tests are ongoing for a similar project. We will also derive a fast digital signal for triggering using a dedicated FPGA logic.

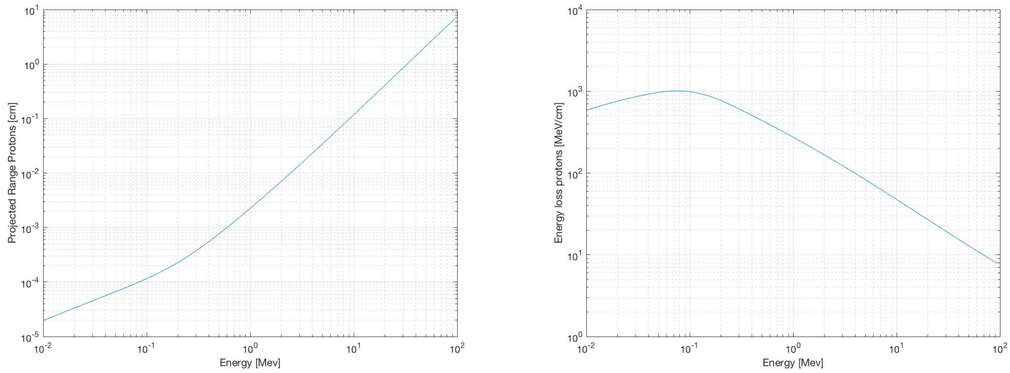

Figure 19: Projected range (left) and specific energy loss (right) for protons in scintillator for different kinetic energies [34].

3.2 Muon measurement

The scattered muon can be identified using the COMPASS spectrometer including the muon identification system present. As mentioned above, the energy transfer in the reaction is very small and falls within the energy resolution of the spectrometer. However, COMPASS has proven excellent angular resolution in the context of a measurement scattering pions of 190 GeV energy off the electromagnetic field of heavy nuclei like Pb or Ni. Despite the presence of a solid target of thickness d $= 20\% X_0$, COMPASS obtained a Q^2-resolution of $\Delta Q^2 = 2 \cdot 10^{-4} (GeV/c)^2$. This was achieved by means of two silicon telescopes placed upstream and downstream of the solid target. The position resolution of each silicon station was about $\Delta x \approx 2\mu m$. Within this set-up, we propose to position the silicon stations within a telescope much further apart ($1m$ providing a longer lever arm. For the purpose of this proposal, we assume that we can improve on the angular resolution such as to achieve a resolution of $\Delta Q^2 = 1.4 \cdot 10^{-4} (GeV/c)^2$ by:

1. replacing the thick solid target with a pressurised gaseous hydrogen target
2. increase the spacing of silicon telescope to roughly match multiple scattering effects in the silicon itself and
3. run with a lower beam energy of 50 GeV to reach the lowest values of Q^2. Muon scattering angles double going from 100 to 50 GeV beam energy.

(**we need simulations to prove these effects**)

3.3 Beam and count rates

We assume the standard COMPASS muon beam at a nominal beam energy of 100 GeV. The beam has the following parameters:

In order to calculate the integrated luminosity for this experiment we make use of the parameters outlined in table 1. Assuming a 35cm long gaseous hydrogen target operated at 4 bar pressure we obtain $L = 4.7 \cdot 10^8 \mathrm{m}b^{-1}$.

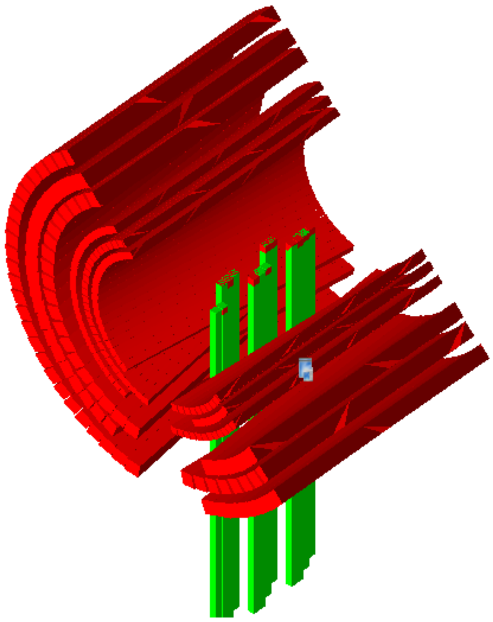

Figure 20: Layout of the active target made from scintillating fibres arranged along the beam direction.

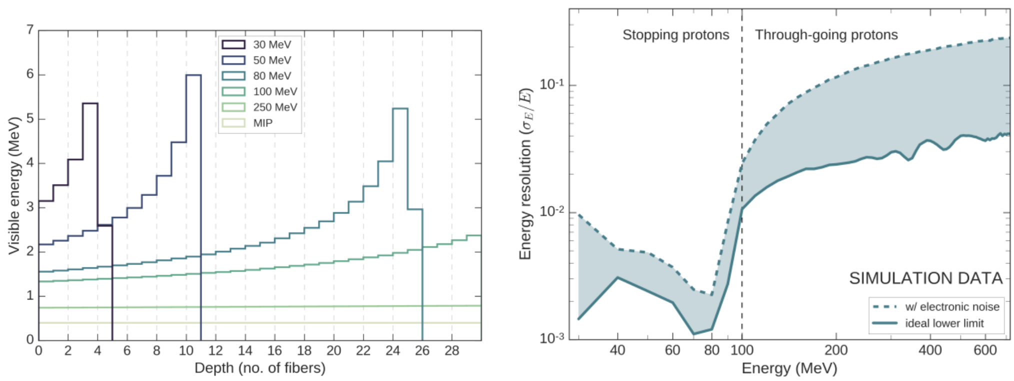

Figure 21: Left: Expected energy loss in individual fibres traversed by recoil protons for different proton energies. Right: energy resolution obtained by Bragg-curve fitting using simulation data. Work in progress and data are still very preliminary

Table 1: COMPASS μ-beam parameters

Energy	100 GeV
$\mu/spill(max)$	$2.7 \cdot 10^8 \mu/spill$
Instantaneous intensity μ/s (scifi trigger)	$5.6 \cdot 10^7 \mu/s$
Instantaneous intensity μ/s (beam trigger)	$2 \cdot 10^5 \mu/s$
spill length	4.8s
mean duty cycle	18%
DAQ, veto deadtimes	0.5
spills per minute	3.3
efficiency of SPS	0.8
effective beam rate	$4 \cdot 10^6 \mu/s$
beam spot size	8x8mm^2
beam divergence	1mrad
total days of beam time	180
beam time for each pressure setting	80
beam time for SciFi target	20
integrated luminosity LH_2 @ 4bar	$1.04{\cdot}10^6 (mb)^{-1}$
integrated luminosity LH_2 @ 20bar	$5.2{\cdot}10^6 (mb)^{-1}$
integrated luminosity SciFi target	$3.7{\cdot}10^9 (mb)^{-1}$

3.4 Trigger

One of the challenges of this experiment is the trigger. Reaching down to low values of Q^2 requires to trigger on signals of low-energy recoil protons. Assuming the TPC to be divided longitudinally into individual cells of length 10cm leads to a constant background noise from beam and halo muons of 20 keV/traversing particle. The drift time of electrons in hydrogen at 4bar is about $10\mu s/cm$, thus $100\mu s$ for 10cm. we may consider two scenarios, one using the full beam intensity and the other one a much reduced intensity, both scenarios being connected to a particular trigger scheme.

- Assuming an instantaneous beam rate of $4 \cdot 10^7 \mu/s$ we expect a continues ionisation signal of about 80 keV within this time window. Therefore, a threshold of about 240 keV must be set (3σ) for triggering. With a mean energy for ion production in hydrogen of about 30eV [29] this corresponds to about roughly 7,500 electrons, which is far above the electronic noise of a possible readout preamplifier[3]. The common drawback for all such trigger schemes is the long trigger latency of $50\mu s$ owing to the long drift time (see appendix A.2). Owing to the thin target, this does not pose a problem for elastic scattering events for trigger thresholds above a few $10^{-5}(GeV/c)^2$ as elastic event rates are below $10^4/s$. However, the present COMPASS readout does not allow for a trigger latency above $2\mu s$ ($4\mu s$, if we half the clock frequency for the readout out via APV). However, this is far below any reasonable drift time in a TPC, unless we reduce the gap-size (drift length) to less than 1 cm.

[3]we may assume the standard COMPASS APV readout for offline analysis which shows a noise of 1,500-2,000 electrons for GEM and silicon detectors, but cannot be used for triggering

- As count rates are not an issue for very low values of Q^2, we might envisage to reduce the beam intensity by a factor 25 for dedicated data takings allowing to strongly reduce pile up. We would run a “simple“ beam trigger and assuming the veto system defining the beam and surrounding target to cut a factor of two (no simulations, juts guess work up to now). As event sizes are very small, we may run with trigger rates of about 100 kHz.This would require a beam rate of $2 \cdot 10^5 \mu/s$. For larger values of Q^2, an active scintillator target could be used.
- For high values of Q^2 ($Q^2 > 3 \cdot 10^{-2}(GeV/c)^2$) corresponding to kinetic energies for recoil protons above 15 MeV and proton ranges above 2.5 mm) we will rely on a trigger from the active target, which can simply be obtained by a cut on the total energy observed in combination with a minimum number of scintillating fibres with signals above threshold. Such a system is presently being designed for space application of such a detector, operating in a self triggering mode.

3.5 Normalisation and Calibration

The key requirement for this experiment is an excellent point-to-point normalisation accuracy of below 0.1% (check this number). Unlike for previous experiment at electron beam accelerators with precision magnetic spectrometer with low solid angle, the COMPASS spectrometer has a full acceptance over the full regions of Q^2. Thus, in principle we can determine the differential cross section without normalising different subsets of measurements. However, this seems impractical as we need to modify the target system/target pressure in order to access the different regions of Q^2 with high individual statistical accuracy. We thus foresee the experiment to be done using two different types of targets and, using the TPC target, to take data with 2–3 different values for the target pressure (see discussion in section 3.6). Owing to the short range of recoil protons with energies below $1MeV$ we envisage performing a very low Q^2 run at a pressure of 1 bar. As the count rates are very high, this run can be performed within a few days. In order to cover range of about $10^{-3} < Q^2 < 3 \cdot 10^{-2}(GeV/c)^2$ we need two long data taking periods at 4 bar and 20 bar. In principle, a precise measurement of the beam intensity and the control of target pressure and temperature should give the corresponding luminosities with very high precision. However, in order to guarantee good matching, we can perform pressure scans. As the pressure scans will be used to calibrate the count rates in the effective overlap regions, the normalising runs can be kept short. A normalising region is defined by the largest values of Q^2 for one pressure regime, for which statistical errors are below 1%. As the count rates for the next pressure setting are much larger, sufficient statistical accuracy can be obtained quickly[4].

Although form factors and thus proton radius can be extracted from the functions dependence of the corrected Q^2 dependent count rates, absolute normalisation of the differential cross section serves as an additional measure of comfort. For this, the luminosity and absolute efficiencies have to be determined. The luminosity determination requires beam flux measurements and determination of the fiducial target thickness. While the latter can be controlled up to very high precision as outlined in appendix A.1, we need to perform the dead time and efficiency corrected beam flux. At low beam

[4]depending on the stability of the system and the quality of the luminosity matching, we might even envisage to slowly scan the region of $10^{-4} < Q^2 < 3 \cdot 10^{-2}(GeV/c)^2$ by slowly stepping up the pressure, thereby optimising beam time.

intensities of $2 \cdot 10^5/s$ as envisaged for the TPC target, this can be achieved using unsegmented scintillation counters. For the high flux measurement with instantaneous intensities of $4 \cdot 10^7/s$, we will use the segmented target fibre system, for which individual count rates should be moderate. Thus, we also omit complex acceptance studies of the active target system.

Last but not least we need a high accuracy for the full reconstruction efficiency.

To which accuracy do we need the absolute normalisation of the cross section ??

Q^2 calibration

Calibration of the absolute Q^2-scale is a key element. As Q^2 can be measured by both muon scattering-angle and proton recoil-energy, we can cross check the relative calibration. The resolution of the scattering angle is solely determined by geometry, position resolution of the silicon detectors, multiple scattering in the target and alignment of the detectors. The latter one can be achieved using through-going muons. We may also cross check luminosity and resolutions using $\mu - e$ scattering occurring as background process. However, electrons will be forward going and thus require a dedicated trigger build from ECAL 2. Such a trigger system has already been set-up and operated for Primakoff measurements at COMPASS. The analysis of $\mu - e$ scattering is even more challenging than $\mu - p$ owing to Bremsstrahlung of electrons all along the spectrometer.

3.6 Precision for the proton radius

Without accounting for trigger and reconstruction inefficiencies we can calculate the precision obtained achievable within COMPASS using the boundary conditions outlined in table 1.

We may now assume a triple experiment, one using a liquid hydrogen TPC using a beam trigger and an instantaneous beam rate of $2 \cdot 10^5 \mu/s$ with two different target pressures, the third a scintillating fibre target of 1cm length **(check values in simulation)** and an instantaneous beam rate of $5 \cdot 10^7 \mu/s$. We assume a transition in Q^2 around Q^2 = 0.3(GeV/c)^2. The cross section, calculate using a dipole form factor, is shown in fig. 25a. The ratio of count rates expected for two scenarios for $\sqrt{< r_e^2 >} = 0.84$ fm and $\sqrt{< r_e^2 >} = 0.88$ fm is shown in fig. 25b. We assume 100 bins equally spaced in $log(Q^2)$ within the range of $10^{-4} < Q^2 < 1$ $(GeV/c)^2$. Statistical errors for each bin stay well below 1%.

4 Radiative corections

We have calculated radiative corrections to the elastic scattering process. The calculations are based on [27] with corrected mass values for the proton, which is considered to be point-like. The corrections include vertex corrections, loop corrections and two-photon exchange as shown in fig. 23. The loop correction also include low mass pion loops (without ρ contributions). The results are displayed in fig. 24a and show these corrections to be of order 1% at low values of Q^2 and (-1)–(-3)% at large values. Thus, these corrections are small compared to the case of electron scattering, as performed

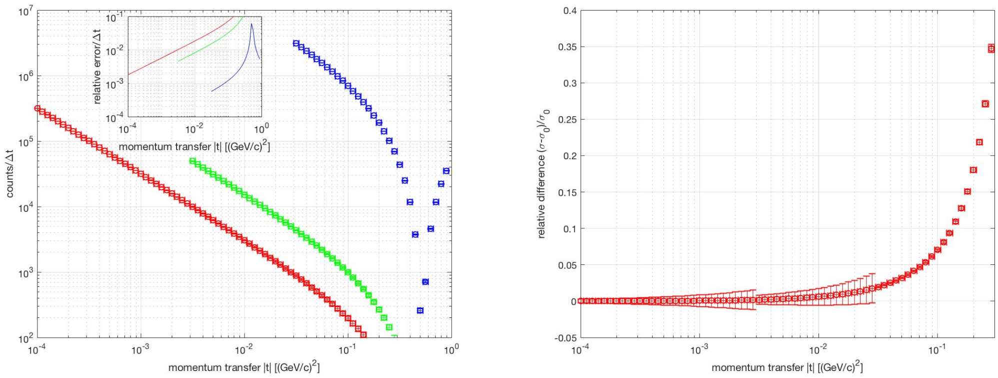

Figure 22: Left: Differential count rate dN/dt for elastic scattering events. The inset shows the relative statistical uncertainties expected. Right: Ratio of two possible scenarios with for $\sqrt{< r_e^2 >} = 0.84$ fm and $\sqrt{< r_e^2 >} = 0.88$ fm (the latter is denoted as σ_0). We assume a triple measurement with three targets.

at low energy accelerators depicted in fig. 24b) for comparison. The results show a logarithmic and thus weak dependence on the effective soft photon cut-off and which can only be determined through detailed simulations and is assumed to be 50 MeV for these calculations (10 MeV for the electron case).

5 Systematic uncertainties

5.1 Magnetic form-factor effects

For extracting the electric form factor and the charge radius, we need to correct for magnetic contributions to the cross section, which grows quickly for $\mathrm{Q}^2 > 0.03\ (GeV/c)^2$. Within our assumption on the form-factor parametrisation, the influence of the magnetic form-factor grows from 6% at $\mathrm{Q}^2 = 0.03(GeV/c)^2$ to as large as 60% at our largest values of $\mathrm{Q}^2 = 0.3(GeV/c)^2$. The magnetic form-factor is known to better than 1%, so the relative uncertainty from the magnetic correction ranges from 0.06% to about 0.6% for the cross sections for the large Q^2 setting. This has to be compared with the size of the effect to be measured, namely the sensitivity of the cross section to the value of the proton radius, being 2% and 30%, respectively. Thus, the uncertainties are small as compared to the required precision.

5.2 Variation of Beam Charge and Energy

The COMPASS beam environment allows for a wide range of systematic studies and we seem to only be limited by the available beam time.

- Ever since the discrepancy in the proton form factors obtained from the Rosenbluth separation and polarisation measurements the discussion of the reliability of the two-photon exchange has been questioned. The two-photon exchange is responsible for the Coulomb cross section being different for equal and opposite charged particle interaction. However, the Olympus collaboration has performed

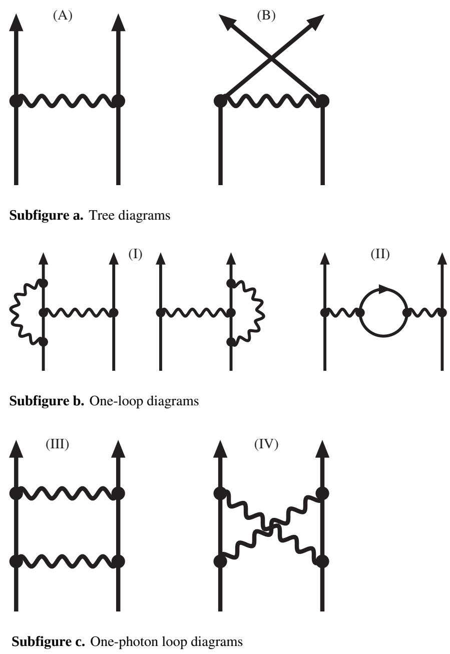

Figure 23: Diagrams contributing to radiative corrections in the μp elastic scattering process. The proton is assumed to be point like. Figure taken from [27].

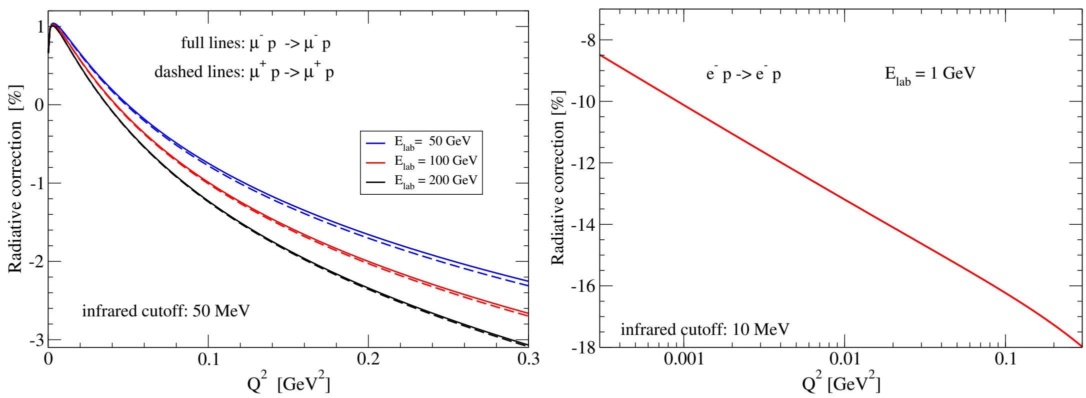

Figure 24: Radiative corrections calculated according to fig. 23. Left: $\mu^{-}p$ for three different values of E_{beam}= 50, 100 GeV, 200 ; right: $e^{-}p$ with E_{beam}= 1 GeV.

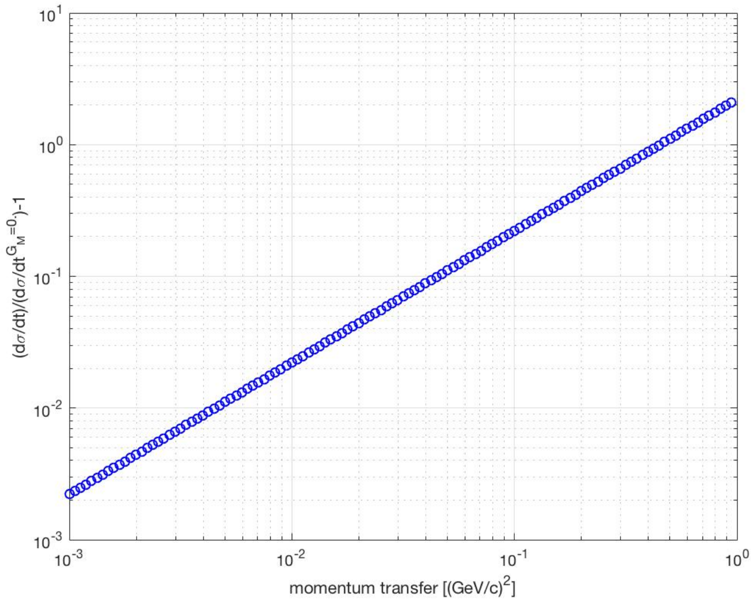

Figure 25: Ratio of elastic cross sections with and without magnetic form factor for different values of Q^2. The cross sections are evaluated using eq. (1) with E_{beam}=100 GeV.

a dedicated experiment comparing electrons and positrons in the last particle physics experiment performed at DESY. They determined the hard two-photon exchange contributions and concluded that the resulting values for the ratio of e^-p to e^+p ($R2\gamma$) are smaller than some hadronic two-photon exchange calculations predict, but are in reasonable agreement with a subtracted dispersion model and a phenomenological fit to the form-factor data [21]. These investigations covered a wide range of virtual photon polarization of $0.456 < \epsilon < 0.978$. Still, the issue has been brought up again in the context of the proton radius puzzle and MUSE has planned for a dedicated measurement.

- As outlined in section 1, lepton universality arguments have been put forward to explain the proton radius puzzle. The arguments for this rather exotic effect have weakened drastically with the redetermination of the Rydberg constant and the subsequent reevaluation of the proton radius from Lamb-shift measurements in electronic hydrogen. Nevertheless, an issue remains in what concerns radiative corrections, which are much smaller for muon induced than for electron induced reaction (see also section 4). COMPASS can perform in situ measurements with high energy electrons (positrons) generated from a γ conversion target placed downstream of T6. A beam of a few $10^5 e^-/s$ may be derived **(Johannes has to verify this number)** and we can repeat the measurements for a small region of low Q^2 (e.g. $Q^2 < 5 \cdot 10^{-3} (GeV/c)^2$ within a shorter beam time.
- The relative accuracy for the determination of Q^2 using the scattered muon depends weakly on Q^2, as muon scattering angles in the laboratory system grow towards lower beam energies (fig. 7). Also radiative corrections depend on the energy of the incoming beam (fig. 24a. However, for the latter only large values of Q^2 are sensitive to the beam energy and thus a systematic study seems beam time consuming.

5.3 Variation of target material

The proposed setup using a high pressure target TPC allows for a rapid change of target material. We can easily exchange hydrogen with deuterium or helium and thus perform a precision measurement of these radii as well. The mean square charge radius of deuterium has recently ben determined using muonic deuterium [22] and further measurements with other elements are planned by the CREMA collaboration [12, 31]. If the proton radius puzzle still persists, it would be highly desirable to also investigate charge radii using muon scattering techniques. Using CH_2 we may also address the carbon charge radius. Discrimination against quasi elastic scattering events can be done as discussed in appendix A.3.

6 Further developments

The present proposal has assumed a rather conservative data taking, which relies on a simple beam trigger and a simple Scifi multiplicity trigger. However, the beam trigger leads to a rather inefficient use of beam time as the beam intensity has to be reduce by a factor 100 as compared to the maximum. This in particular affects the high Q^2 data points for each individual target setting, which in turn determines the beam time required. Two scenarios could in principle be envisaged:

- Recoil proton trigger:
- Scattered muon trigger: The challenge is to detect a small scattering angle of the muon in real time with a maximal latency of $0.5\mu s$. At present, all micro pattern detectors are equipped with the APV readout chip, which has a pipelined architecture and requires a readout time of .. $0.5\mu s$. For the four silicon stations, such a system would have to replaced in favour of a parallelised system, which feeds its data into a FPGA array. The track reconstruction algorithm is then required to single out noise and reconstructs relative angle of incoming and outgoing beam particle track. As such a trigger would only be necessary for $Q^2 > 10^{-3}(GeV/c)^2$, where the scattering angle exceeds $300\mu rad$ such that alignment on the hourly basis is not required.

7 Experimental Requirements

The apparatus requirements imposed by these new measurement are rather modest, but do require additional detectors. These concern the target TPC and the SciFi active target recoil detector. As the determination of the muon scattering is vital, we have to refurbish at least one silicon station. In addition, we need longer optical benches to achieve internal stability for both silicon telescopes and minimise thermal displacements. Although the beam is very pure with a pion contamination below 10^{-5} we should install a muon filter at the downstream end of the COMPASS experiment. The installation of new detectors also imposes requirements on new electronics and their implementation into the COMPASS DAQ scheme.

Detector	Responsibility	needed [y/n]	new/old
μ Beam	CERN	y	old
electron Beam	CERN	y ?	new
BMS		y	old
Siilicon telescopes	TUM	y	old
Silicon station	TUM +++	y	new
TPC and pressure tank	Gatchina	y	new
TPC gas system	Gatchina	y	new
TPC RO	Gatchina, Bonn ISKP, Freiburg ++	y	new
SciFi target	TUM++	y	new
SciFi tracker		y	old
GEM	Bonn ISKP ++	y	refuribshed
Micromega	Saclay ? ++	y	old
Straws	-	n	
MWPC	-	n ?	
DC	-	n ?	
RICH	-	n	
HCAL	-	n	
ECAL 0	-	n	
ECAL 1	-	y for e-beam	
ECAL 2	-	y for e-beam	
MW1	-	n	
MW2	-	n/y ?	
W45	-	n	
DAQ	TUM, Prague ++	y	
Trigger	Bonn PI, Mainz ++	y	
Slow control	Lisbon	y	
Online analysis		y	
Installation	CERN		

Table 2: **tentative and very preliminary** Requirements and responsibilities for equipment

8 New Collaborators

The proposal extends the physics scope of COMPASS and thus would allow to attract new collaborating groups: The group of PNPI Gatchina, experienced in active high pressure hydrogen targets has expressed strong interest to join COMPASS for this measurement. This group has performed radius measurement at GSI [26], contributed with a high pressure hydrogen TPC for the MUCAP experiment at PSI [23, 24] and plans for further employment of their technology at FAIR. They are also key players for the new letter of intent using this technology at MAMI.

References

[1] R. Hofstadter and R. W. McAllister, Phys. Rev. **98** (1955) 217. doi:10.1103/PhysRev.98.217
R. W. Mcallister and R. Hofstadter, Phys. Rev. **102** (1956) 851. doi:10.1103/PhysRev.102.851

[2] R. Pohl [CREMA Collaboration], "The Lamb shift in muonic hydrogen and the proton radius puzzle," Hyperfine Interact. **227** (2014) no.1-3, 23. doi:10.1007/s10751-014-1011-1

[3] R. Pohl *et al.*, "The size of the proton," Nature **466** (2010) 213. doi:10.1038/nature09250

[4] J. C. Bernauer, "Precise form factors from elastic electron scattering," J. Phys. Conf. Ser. **381** (2012) 012006. doi:10.1088/1742-6596/381/1/012006

[5] A. Antognini *et al.*, "Experiments towards resolving the proton charge radius puzzle," EPJ Web Conf. **113** (2016) 01006 doi:10.1051/epjconf/201611301006 [arXiv:1509.03235 [physics.atom-ph]].

[6] M. Mihovilovic *et al.*, "First measurement of proton's charge form factor at very low Q^2 with initial state radiation," Phys. Lett. B **771** (2017) 194 doi:10.1016/j.physletb.2017.05.031 [arXiv:1612.06707 [nucl-ex]].

[7] A. H. Gasparian [PRad Collaboration], "The New Proton Radius Experiment at Jefferson Lab," JPS Conf. Proc. **13** (2017) 020052. doi:10.7566/JPSCP.13.020052

[8] R. Pohl *et al.*, "Deuteron charge radius and Rydberg constant from spectroscopy data in atomic deuterium," Metrologia **54** (2017) L1 doi:10.1088/1681-7575/aa4e59 [arXiv:1607.03165 [physics.atom-ph]].

[9] T. Suda, "Electron scattering experiment off proton at ultra-low Q^2,"
http://www2.yukawa.kyoto-u.ac.jp/∼min2016/slides/Suda_MIN2016.pdf,
talk presented at Meson in Nucleus conference, Kyoto, 2016.

[10] R. J. Hill, "Review of experimental and theoretical status of the proton radius puzzle," EPJ Web Conf. **137** (2017) 01023 doi:10.1051/epjconf/201713701023 [arXiv:1702.01189 [hep-ph]].

[11] J. J. Krauth *et al.*, "The proton radius puzzle," arXiv:1706.00696 [physics.atom-ph].

[12] R. Pohl for the *CREMA collaboration*, "Shrinking the Proton," presentation at the PhiPsi2017 workshop at Mainz, June 2017.

[13] R. Pohl *et al.*, Metrologia **54** (2017) L1 doi:10.1088/1681-7575/aa4e59 [arXiv:1607.03165 [physics.atom-ph]].

[14] J. C. Bernauer and M. O. Distler, "Avoiding common pitfalls and misconceptions in extractions of the proton radius," arXiv:1606.02159 [nucl-th].

[15] P. Mergell, U. G. Meissner and D. Drechsel, "Dispersion theoretical analysis of the nucleon electromagnetic form-factors," Nucl. Phys. A **596** (1996) 367 doi:10.1016/0375-9474(95)00339-8 [hep-ph/9506375].

[16] I. T. Lorenz, H.-W. Hammer and U. G. Meissner, "The size of the proton - closing in on the radius puzzle," Eur. Phys. J. A **48** (2012) 151 doi:10.1140/epja/i2012-12151-1 [arXiv:1205.6628 [hep-ph]].

[17] R. Gilman *et al.* [MUSE Collaboration], "Studying the Proton "Radius" Puzzle with μp Elastic Scattering," arXiv:1303.2160 [nucl-ex].

[18] J. Bernhard, responsible for the M3 beam line at CERN, private communication

[19] N. Kaiser, TU Munich, private communication.

[20] C. Adolph *et al.* [COMPASS Collaboration], "Measurement of the charged-pion polarizability," Phys. Rev. Lett. **114** (2015) 062002 doi:10.1103/PhysRevLett.114.062002 [arXiv:1405.6377 [hep-ex]].

[21] B. S. Henderson *et al.* [OLYMPUS Collaboration], "Hard Two-Photon Contribution to Elastic Lepton-Proton Scattering: Determined by the OLYMPUS Experiment," Phys. Rev. Lett. **118** (2017) no.9, 092501 doi:10.1103/PhysRevLett.118.092501 [arXiv:1611.04685 [nucl-ex]].

[22] R. Pohl *et al.* [CREMA Collaboration], "Laser spectroscopy of muonic deuterium," Science **353** (2016) no.6300, 669. doi:10.1126/science.aaf2468

[23] J. Egger *et al.*, "A high-pressure hydrogen time projection chamber for the MuCap experiment," Eur. Phys. J. A **50** (2014) no.10, 163 doi:10.1140/epja/i2014-14163-1 [arXiv:1405.2853 [physics.ins-det]].

[24] S. M. Clayton, "The MuCap Experiment," AIP Conf. Proc. **1222** (2010) 407. doi:10.1063/1.3399355

[25] A. A. Vorobyov, G. A. Korolev, V. A. Schegelsky, G. Y. Solyakin, G. L. Sokolov and Y. K. Zalite, "A method for studies of small-angle hadron-proton elastic scattering in the coulomb interference region," Nucl. Instrum. Meth. **119** (1974) 509. doi:10.1016/0029-554X(74)90801-5

[26] S. Ilieva *et al.*, "Nuclear-matter density distribution in the neutron-rich nuclei 12,14 Be from proton elastic scattering in inverse kinematics," Nucl. Phys. A **875** (2012) 8. doi:10.1016/j.nuclphysa.2011.11.010

[27] N. Kaiser, "Radiative corrections to lepton-lepton scattering revisited," J. Phys. G **37** (2010) 115005. doi:10.1088/0954-3899/37/11/115005

[28] Gorur Govinda Raju, “Gaseous Electronics: Theory and Practice,” CRC Taylor and Francis, 2005

[29] B. E. Leonard and John W. Boring, “The Average Energy per Ion Pair, W, for Hydrogen and Oxygen Ions in a Tissue Equivalent Gas,” Radiation Research, Vol. 55, No. 1 (Jul., 1973), pp. 1-9

[30] M. J. Losekamm, M. Milde, T. Pöschl, D. Greenwald, and S. Paul, “Real-Time Omnidirectional Radiation Monitoring on Spacecraft,” in AIAA SPACE 2016, American Institute of Aeronautics and Astronautics, 2016.
M. J. Losekamm, T. Pöschl, D. Gaisbauer, D. Greenwald, and S. Paul, “AFIS: A New Instrument for Cosmic Radiation Studies on BEXUS 18 and Future Nanosatellite Missions,” in 22nd ESA Symposium on European Rocket and Balloon Programmes and Related Research, 2015.
T. Pöschl, M. J. Losekamm, D. Greenwald, and S. Paul, “A Novel CubeSat-Sized Antiproton Detector for Space Applications,” in 34th International Cosmic Ray Conference, 2015.
M. J. Losekamm, T. Pöschl, M. Langer, and S. Paul, “The AFIS Detector: Measuring Antimatter Fluxes on Nanosatellites,” in 65th International Astronautical Congress, 2014.
A. Hahn, “Charakterisierung von Silizium Photomultipliern zur Auslese von szintillierenden Fasern,” bachelor thesis, Technical University of Munich, 2014.
L. Meng, “Development of a CubeSat Detector for Measuring the Low-Energy Antiproton Flux in Low Earth Orbit,” master thesis, Technical University of Munich.

[31] Biraben, F. et al, CREMA collaboration,
“Proposal for an experiment at PSI: Lamb shift in muonic helium,”
https://www.ethz.ch/content/dam/ethz/specialinterest/phys/particle-physics/precisionphysicsatlowenergydam/Research/Proposal_muHe_pdf.pdf

[32] V. A. Ganzha *et al.*, “A Circulating hydrogen ultra-high purification system for the MuCap experiment,” Nucl. Instrum. Meth. A **578** (2007) 485 doi:10.1016/j.nima.2007.06.010 [arXiv:0705.1473 [nucl-ex]].

[33] J. J. Lowke and J. H. Parker, “Theory of Electron Diffusion Parallel to Electric Fields. 2. Application to Real Gases,” Phys. Rev. **181** (1969) 302. doi:10.1103/PhysRev.181.302

[34] Values for stopping power and energy loss in hydrogen are taken from https://www.nist.gov/pml/radiation-dosimetry-data

A Appendix

A.1 Details on the TPC

The design of the TPC is motivated by the exact knowledge of the fiducial volume for reconstructable elastic scattering events. This requires high precision on the gas density and geometrical parameters, the exact characterisation of the active TPC volume.

Driftspace: in order to shape the drift field, twenty field correction rings are placed in the outer TPC region between the cathode and the grid to form the uniform electric field in the drift space. the high voltage distribution includes -100 kV on the Cathode, -7 kV on the Grid, 0 kV on the anode at 20 bar pressure. The HV is distributed for the field compensating rings with a resistor divider. The HV will be known with 0.01% absolute precision.

H_2 gas purity: in order to avoid the losses of the ionisation electrons during the drift time, the contamination of the H_2 gas by any electro-negative gas (O_2, H_2O) should be reduced to a level below 1 ppm. This will be achieved by continuous H_2 purification with a special gas purification system, similar to that described in [32], which eliminates gas impurities down to smaller than 0.1ppm.

Number density: the number n of protons per cm^3 in hydrogen gas depends on the pressure p_{tech} and temperature t_0. We will control the pressure to 0.01% absolute precision and keep the temperature constant to a level ±0.050 (0.014% absolute precision). This determines the proton density with 0.025% absolute precision.

Time, recoil energy, and recoil angle resolution: the anode channels will be equipped with low noise preamplifiers with the noise at the level of 20 keV (σ). Such numbers can be achieved using a custom made preamp (Gatchina) or by the SAMPA ASICs developed for the ALICE TPC upgrade (ENC: 680 e^- noise).- This determines the recoil energy resolution. Depending on the range of the recoil proton, the recoil energy is obtained by the sum of energies deposited against the anode pixels. Accordingly, the noise will be summed up as well. So the energy resolution for maximal proton range ($T_{rec} \sim 10\ MeV$ for 20 bar, $T_{rec} \sim 4\ MeV$ for 4 bar) will be around $\sigma_E \sim 60\ keV$. Note, however, that the noise might be larger in the presence of the muon beam and strongly depends on the segmentation of the anode plane.

The expected signal arrival time resolution is $\sigma_t = 40ns$[5]. The angular resolution σ_{θ_R} is limited by Coulomb scattering of the recoil protons with $\sigma_{\theta_R} \sim 10$ mrad. θ_R is measured by the differences in arrival times of the signals from the anode pixels crossed by the recoil. The precision of such measurements varies from $\sim \pm 10$ mrad (signals from two neighbouring pixels) to $\sim \pm 2$ mrad for long ranged protons. So the final recoil angle resolution will be from 15 mrad to 10 mrad (for proton range $60 - 80$ mm and ~ 300 mm, respectively).

Electron drift velocity and track diffusion in TPC: The electron drift velocity is $v_1 \approx 0.42$ cm/μs in the TPC drift region and $v_1 \approx 0.75$ cm/μs in the region of the anode-grid. The value of v_1 should be known with high precision (better than 0.1%) as it determines the fiducial gas target thickness (important for absolute cross section measurement) and determines the z-coordinate of the interaction point. The value of v_1 will be measured in special measurements at MAMI by detecting time intervals between the beam trigger and the signals produced by beam electrons crossing TPC perpendicular to the TPC axis at three z- coordinates counted from the the HV plane: z=10 mm, z=200 mm, and z=380 mm. Three Be-windows in the TPC body will be arranged at these distances. The whole setup should be turned by 90°for these measurements. The distances between the selected z-coordinates will be determined with 20 μm precision by precision shifting the setup across the beam direction. The expected precision in measurements of the drift velocity is 0.01%. Such measurements could be repeated at COMPASS using the silicon telescopes surrounding the target TPC.

[5]at present, we do not have the time resolution for the option of the SAMPA ASICs

The same measurements will provide information on track diffusion during the drift time by observation of the TPC signal width in function of the drift time. According to the available literature information [33], the track diffusion is rather small. In our experimental conditions it should be $\sigma_L \approx 0.006\sqrt{L}$, that is $\sigma_{diff} \sim 280\mu m$ for maximum drift distance $L = 20cm$. The diffusion is not important for measurements of v_1 where arrival time will be determined by the signal maximum. But it may have some effect on measurement of arrival times of the TPC signals which will be determined by the leading edge of the signals. In this case, some small corrections to the measured arrival times may be needed, which will be obtained from the diffusion measurements, mentioned above. The drift velocity depends on the ratio E/P (electric field / pressure) in the drift space. A change in E/P by 1.5% changes the drift velocity by 1%. In our experiment, both HV and the pressure will be kept stable and reproducible at a level of 0.02%. The drift velocity measurements will be performed at different values of the high voltage, HV=100 kV, 95kV, and 90 kV. Similar measurements will be performed at 4 bar pressure with the HV reduced by a factor of five.

Gas target length: the gas target length, L_{tag}, is determined from the measured difference between maximal and minimal arrival times of the TPC signals in the chosen drift space, $L_{tag} = (t_{arr}^{max} - t_{arr}^{min}) \cdot v_1$. Only a small correction to t_{arr}^{max} might be needed for track diffusion. The expected precision in L_{tag} determination is 0.02% **(check numbers... the quoted precision was mentioned for L = 35cm)** for $L_{tag} = 20cm$.

Vertex z coordinate - Calibration and resolution: calibration of the z-scale will be done simultaneously with measurements of the drift velocity at the electron beam at MAMI. For this, the TPC setup will be slightly turned so that the electron beam (in position z=10 mm) will cross the HV plane in the TPC central region thus producing ionisation at z close to z=0. Registration of these signals can fix the z scale in TPC with absolute precision better than 100 μm. Care has to be taken to account for the difference in electronic delays between the beam trigger and TPC signals at the calibration and main experiments. Another way to determine z = 0 can be the in situ detection of the beam muon signals on the central anode in the nominal zero degree TPC position. The z=0 point can be found by analysing the trailing edge of these $\sim 100\mu s$ **(our signals should be shorter)** long signals. Advantage: such measurements can be done at any time in the course of the main experiment (with beam intensity reduced to $10^3 \mu/s$). The main disadvantage is relatively large systematic uncertainty determining the z=0 point. The optimal solution would be calibration of this method again by the 90°setup measurements. Then it can be used as a stability control for the z scale calibration in the course of the experiment. As to the longitudinal z resolution in detection of the recoil protons, it depends on the arrival time resolution. The z-resolution is expected to be $\sigma_z \sim 200\mu m$.

A.2 Drift in gaseous hydrogen

(requires corrections of values to be consistent with Gatchina numbers)
For exercise we shall assume a total drift path in the TPC of 10 cm with a field applied of 10kV resulting in an electric field strength of 1kV/cm. At a pressure of 4 bar, the number density of hydrogen atoms is about $2.14 \cdot 10^{21} cm^{-3}$ and thus E/N becomes $5 \cdot 10^{-19} V cm^2$ or $5 \cdot 10^{-2}$ Td. According to fig. 26, the drift velocity for electrons is $v_e = 1mm/\mu s$ and hydrogen ions travel with roughly $10^{-4} cm/\mu s$. Thus, the maximal

drift time for electrons becomes $100\mu s$ and ions build up over $\tau_{H^+} = 0.1s$. Assuming an instantaneous beam intensity of $I_\mu = 4 \cdot 10^7 \mu/s$ and an energy loss of $E_{loss} = 20keV$, with $W_I = 30eV$ per ion pair produced, we obtain:

$$N_{H^+} = I_\mu \cdot \frac{E_{loss}}{W_I} \cdot \tau_{H^+} = 0.88 \cdot 10^9 \tag{4}$$

hydrogen ions in the drift volume over the time of a spill.

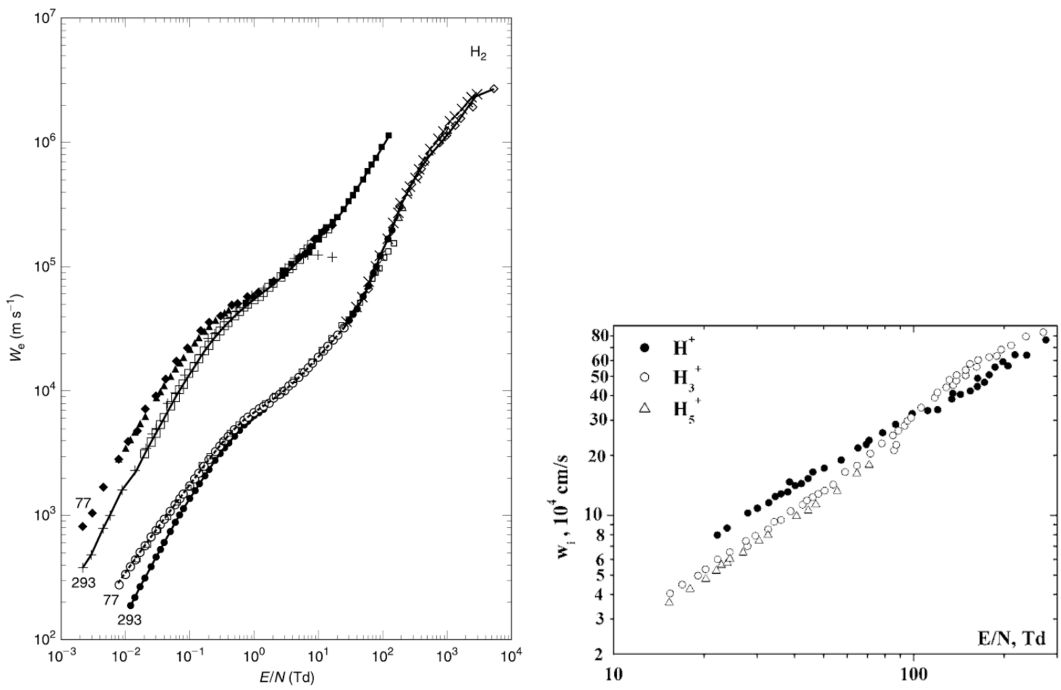

Figure 26: Drift velocities for electrons and protons in hydrogen and deuterium (scaled by a factor 10) [28]. Note that 1Td = E/N corresponds to $10^{-17} V \cdot cm^2$ and $N = 5.4 \cdot 10^{20} cm^{-3}$ at 1 atm.

A.3 Background from quasielastic scattering off carbon

Owing to the low muon beam intensity in COMPASS, elastic scattering at high Q^2 can only be performed using solid targets with densities of order one. In section 3.2 we outlined the use of an active target made from scintillating fibres. For the sake of simplicity we assume a stocheometric composition of $(CH)_n$. The presence of carbon leads to quasielastic scattering off bound protons being about six times as frequent as on hydrogen. The quasi elastic kinematics leads to a shift of the elastic peak by the binding energy of about 8 MeV and a broadening due to Fermi motion. These background reactions have to be strongly suppressed using the measurement of the recoil proton energy and momentum vector and the recoil kinematics has to be matched with the kinematics of the scattered muon, from which we determine Q^2 .

In order to estimate kinematic distributions for quasi elastic scattering, we have performed simulations, assuming a Gaussian momentum distribution of bound protons with a width of 200 MeV/c. Figure 27a shows, that Fermi energies exceed recoil proton energies up to kinetic energies of 0.8 GeV/c, roughly corresponding to $Q^2 > 1(\mathrm{GeV/c})^2$ (see fig. 9). Exemplarily we compare the x-component (transverse) of the recoil proton momentum with and without Fermi momentum superimposed fig. 27b). The smearing of recoil proton kinematics changes the value of Q^2 extracted from the recoil proton as shown in fig. 28a. This scalar property is complemented by a directional change of the recoil proton as compared to the original scattering kinematics on both azimuth $\Delta\phi$ and polar $\Delta\theta$ angles (fig. 28b)). As the polar angle for recoil protons is small for elastic scattering and the effect of Fermi motion enlarges this angle there is a shift of the distribution of away $\Delta\theta$ from zero towards larger polar angles.

However, the change in kinematics is only sizeable at lower values of $Q^2 < 0.5$ $(\mathrm{GeV/c})^2$, as is depicted in fig. 30d) and e), which shows the change of recoil proton polar angle and energy due to Fermi motion and nuclear binding energy.

Quasielastic scattering can now be rejected by comparing the values of Q^2 reconstructed from the outgoing muon and recoil proton (measuring E_{kin}). Most quasi elastic scattering events can be rejected by this. Owing to the nuclear binding, this also causes an effective cut-off for quasi elastic scattering events with $Q^2 < 0.1(\mathrm{GeV/c})^2$. Remaining quasi elastic events can be eliminated by requiring transverse momentum balance of muon and recoil proton. **??** shows the Q^2 distribution after each step of selection: a) requirement of recoil proton energy to be within 10% of the expected from muon scattering angle; b) requirement of measured recoil proton azimuth to be within 100 mrad off expectation ;c) recoil proton polar angle to be within 100 red of expectation. Each selection step removes about 90% of remaining quasi elastic events.

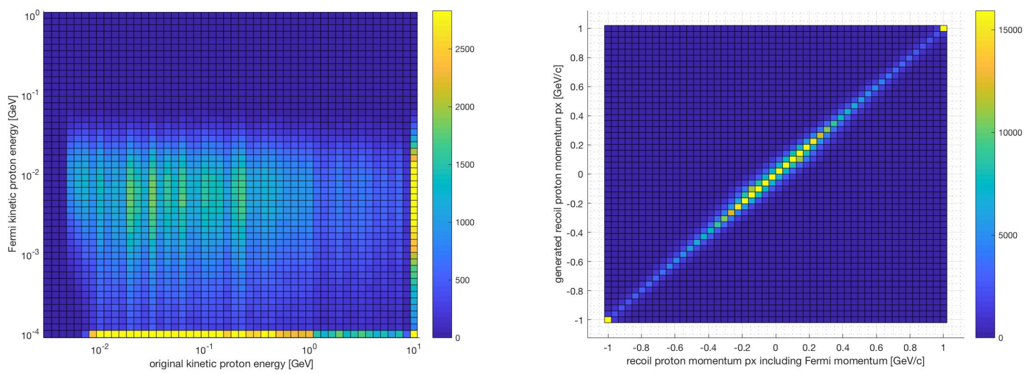

Figure 27: Left: Distribution of Fermi energies for different recoil proton energies. Right: transverse x-component of the recoil proton momentum with and without Fermi momentum superimposed.

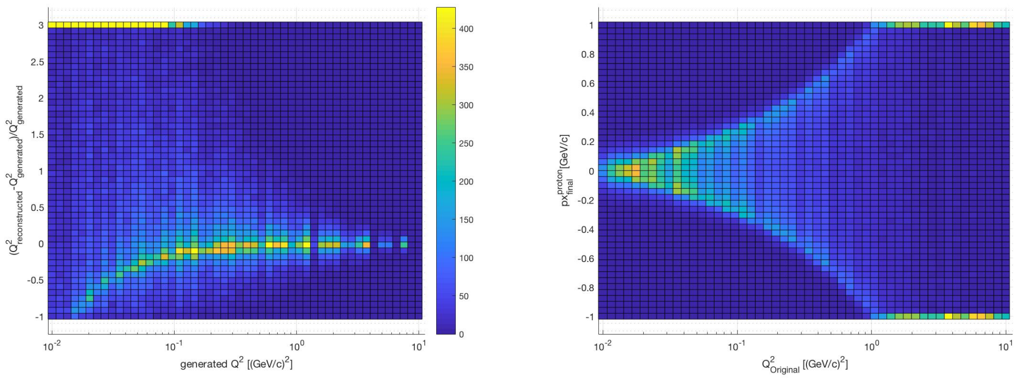

Figure 28: Left: smearing of polar and azimuth angle for the recoil proton. Right: transverse x-component of the recoil proton momentum with and without Fermi momentum superimposed.

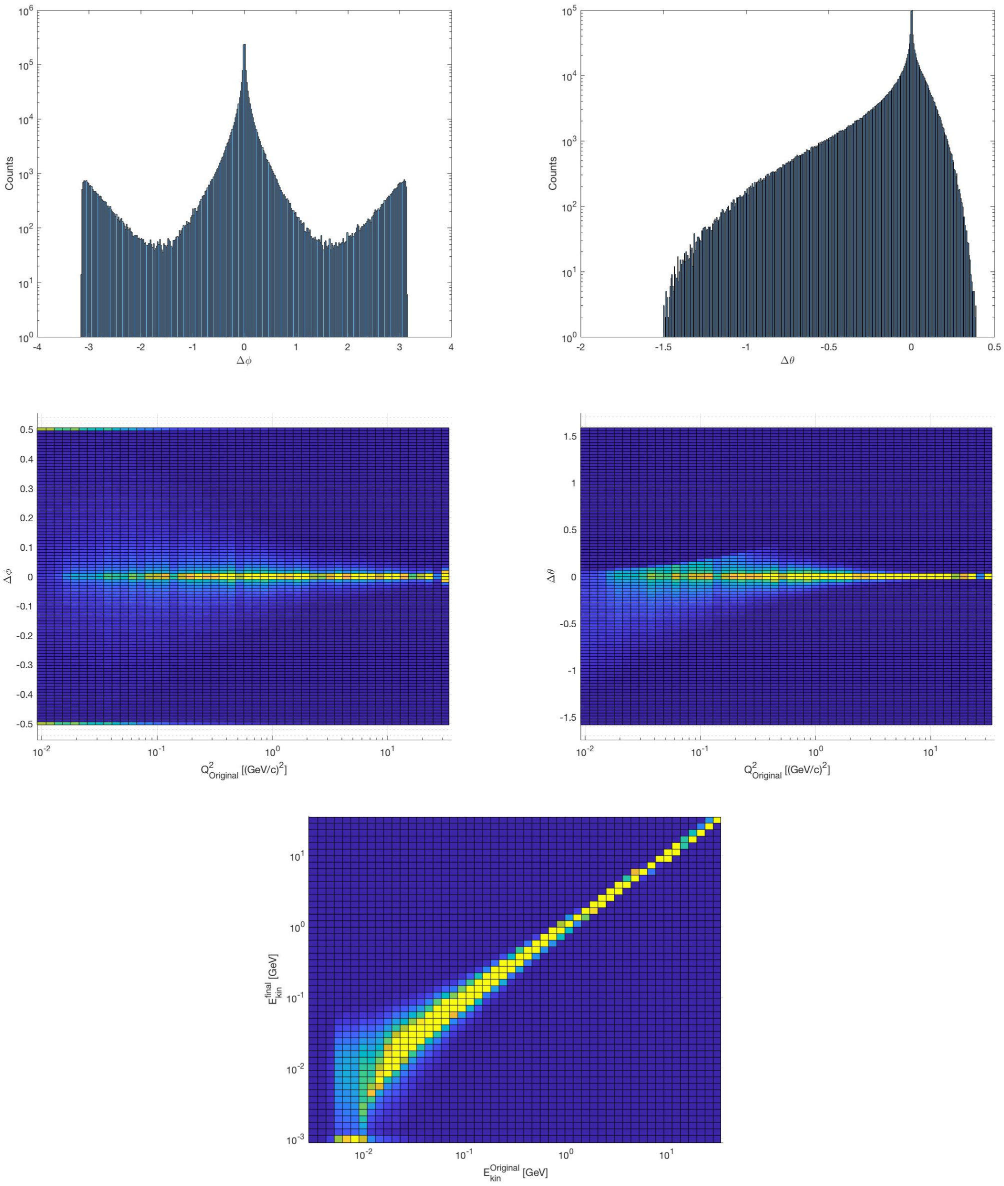

Figure 29: Change of azimuth and polar angle in scattering kinematics for quasi-elastic scattering. Upper row: $\Delta\theta$ (left) and $\Delta\phi$ (right) over all Q^2- Lower row: left: correlation of $\Delta\phi$ vs $\Delta\theta$; right: $\Delta\phi$ vs. Q^2

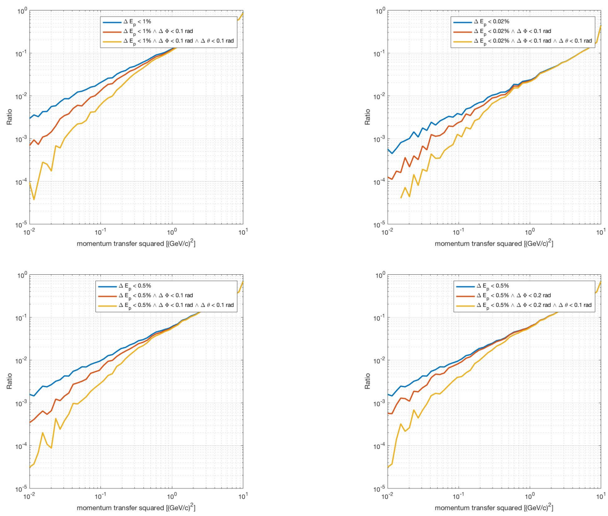

Figure 30: Q^2 dependent supression of quasi elastic scattering events with different assumptions on energy and angular resolutions. Each set of curves depicts consecutive application of selection in recoil proton energy, azimuthal and polar angle of emission.